# A Nonuniform Sampling Lifetime Estimation Technique for Luminescent Oxygen Measurements

Ian Costanzo, Devdip Sen, John McNeill, Ulkuhan Guler

Electrical and Computer Engineering Department, Worcester Polytechnic Institute, Worcester, MA, USA
imcostanzo@wpi.edu, uguler@wpi.edu

Abstract—This paper presents a nonuniform sampling technique for measuring the lifetime of luminescent materials for oxygen sensing. The system features a switched-capacitor circuit to implement fixed-voltage steps for quantization, enabling long integration times without saturating the front-end amplifier. A control circuit automatically tunes the light emitting diode (LED) excitation pulses to avoid overpowering or starving the front end as photodiode current varies with changes in the partial pressure of oxygen. Time gating of the front-end integrator removes the need for optical filtering. The analog front end (AFE) has a gain bandwidth product of 10 MHz and an input-referred noise of 124  $\mu V_{rms}$  (measured 200 Hz - 100 kHz). The circuit was realized in 180 nm CMOS technology. The AFE and LED driver consume a maximum of 16  $\mu J$  per calculation. We have demonstrated the entire system's functionality by measuring oxygen concentrations from 0 to 240 mmHg in a controlled gas vessel. The results indicate satisfactory linearity on a Stern-Volmer plot covering the human-relevant range of 50 to 150 mmHg.

Index Terms—Oxygen sensor, nonuniform sampling, luminescent measurements, transcutaneous sensing, blood gases.

### I. INTRODUCTION

The ability to monitor the respiration of at-risk patients in real-time at home is critical to preventing respiratory failures. Care providers can assess the effectiveness of respiration by measuring blood gases, namely oxygen  $(O_2)$  and carbon dioxide  $(CO_2)$  [1]. Recently, luminescent gas sensing has reemerged as an attractive method to create miniaturized noninvasive transcutaneous blood gas monitors [2]–[6]. These medical devices measure the partial pressure of  $O_2$  and  $CO_2$  molecules diffusing through the skin, directly correlated with arterial  $O_2$  and  $CO_2$  [1]. The efforts in the field are new, requiring specialized analog front ends (AFE) with lightweight estimation algorithms for accurate sensor readings.

This work presents a nonuniform sampling technique and an offset immune luminescent lifetime estimation algorithm for O<sub>2</sub> sensing. The partial pressure of O<sub>2</sub> (PO<sub>2</sub>) closely correlates with the lifetime of the luminescence quenched by O<sub>2</sub> [7]. Lifetime measurements are preferred over intensity measurements because of their robustness to factors such as variations in the optical path, reducing the vulnerability to motion artifacts and skin color differences [7].

The presented system 1) features a specialized AFE that obtains the luminescent lifetime information and 2) leverages time-gated excitation, removing the need for optical filters to extract the luminescent response from the excitation light. The lifetime  $(\tau)$  is calculated with 3) the proposed offset immune algorithm using the time differences between equal

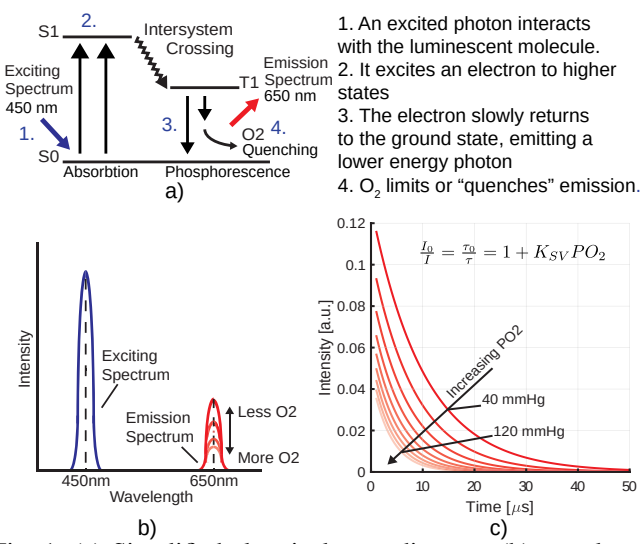


Fig. 1: (a) Simplified electrical state diagram, (b) wavelength shift, (c)  $\tau$  and intensity of the emission quenched by O<sub>2</sub> [8].

voltage steps. 4) The measured mean error is as accurate as 1.9% without post-processing. 5) The system is showcased by measuring the  $PO_2$  in a gas vessel.

The rest of the paper is organized as follows. Section II introduces the basics of luminescent  $O_2$  sensing and explains the proposed lifetime estimation algorithm. Section III describes the hardware implementation. Section IV discusses the measurement results. Section V concludes the paper.

# II. LUMINESCENT OXYGEN SENSING AND LIFETIME ESTIMATION ALGORITHM

Fig. 1 illustrates the basics of the luminescent  $O_2$  sensing mechanism. The  $O_2$ -sensitive dye consists of functional groups known as luminophores. When the luminophores are exposed to relatively high-energy photons (450 nm), electrons in the luminophores jump to higher energy levels. After some time, the electrons try to return to the ground state. For luminescent materials, the excited electrons can enter a triplet state, preventing the electron from returning directly to the ground state. When the electron returns to the ground state from this triplet state, a photon of a longer wavelength is emitted (650 nm). This emission is "quenched" or suppressed by  $O_2$  [9]. The dynamics of this interaction are described by the Stern-Volmer equation, shown inside of Fig. 1c. The intensity (I) and  $\tau$  are related to  $PO_2$  through a rate constant,  $K_{SV}$  and intensity/lifetime with no oxygen ( $I_0/\tau_0$ ).

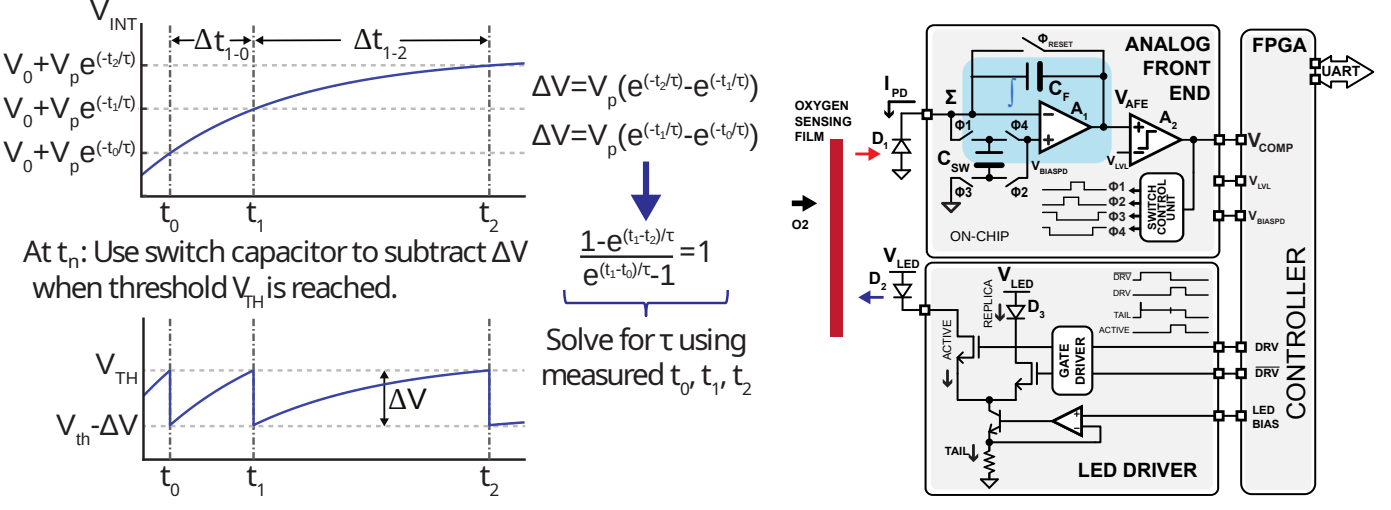


Fig. 2: Lifetime estimation algorithm.

Fig. 3: Diagram of the O<sub>2</sub> measurement system.

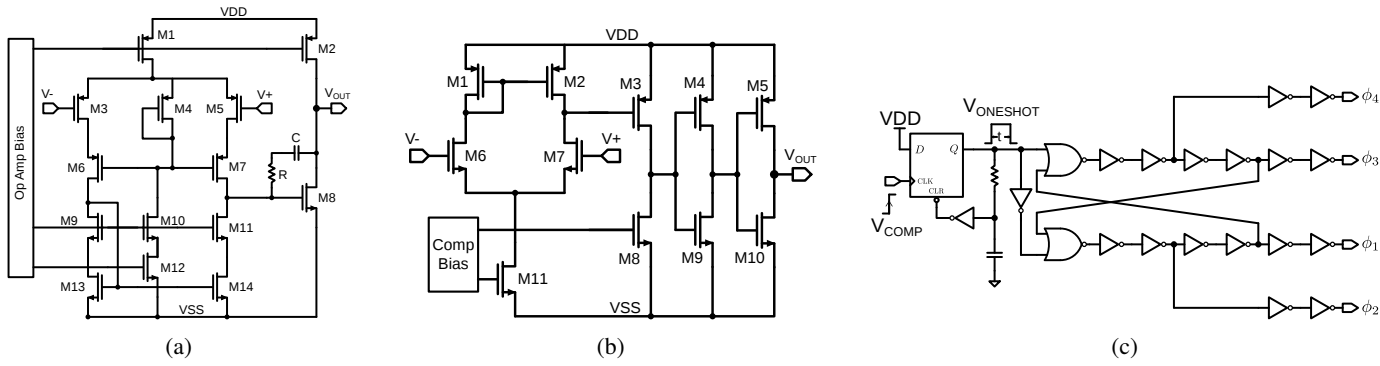


Fig. 4: Simplified schematics of (a) front-end amplifier A<sub>1</sub>, (b) comparator A<sub>2</sub>, (c) switch control unit.

Fig. 2 visualizes the proposed lifetime estimation algorithm. We use the time differences  $(\Delta t)$  between fixed-voltage steps  $(\Delta V)$  to extract the time constant  $(\tau)$  of the decaying exponential. This algorithm, easily realizable in hardware, is a modification of rapid lifetime determination [10]. The integration of an exponential does not change the time-constant  $(\tau)$ , the key parameter we want to measure. Integrating the current generated by the photodiode captures the exponential signal. When the integrated signal voltage reaches a pre-set threshold, the system records the time of the level crossing (e.g.,  $t_0$ ,  $t_1$ ), and the integration proceeds without interruption.

Taking the difference between two level crossings eliminates the integration constant, as seen in Fig. 2. This operation removes any offset errors in the system. The quotient of two differences removes the amplitude component of the exponential. The result is a transcendental equation that is only dependent on the level crossings' sample times,  $t_0$ ,  $t_1$ , and  $t_2$ , and the unknown luminescent time constant,  $\tau$ . A basic root-finding algorithm calculates  $\tau$  within a few iterations. This lightweight, offset immune algorithm requires only three samples, relaxing the data rate requirements.

# III. SYSTEM ARCHITECTURE

Fig. 3 shows a diagram of the nonuniform sampling system. The system's operation is divided into an excitation phase and a readout phase. During the excitation phase, the light-

emitting diode (LED) driver creates a pulse at a set intensity and duration, exciting the  $O_2$ -sensitive film with blue light ( $\lambda = 450nm$ ). The integrator,  $A_1$  and  $C_F$ , is set to unitygain with a switch ( $\phi_{RESET}$ ) to avoid saturating the AFE with the high-intensity LED burst.  $C_F$  is only reset during the excitation phase, minimizing the impact of reset noise. In addition, the time-domain signal gating via  $\phi_{RESET}$  removes the need for optical filtering to extract the relatively weak luminescent signal from the powerful excitation signal.

In the readout phase, a photodiode,  $D_1$ , captures the emitted red photons ( $\lambda=650nm$ ), generating a current ( $I_{PD}$ ) that matches the decay of the photons, depicted in Fig. 7c.  $A_1$  and  $C_F$  integrate this current to generate a voltage. The integrator is assisted with a nonuniform switched-capacitor technique to improve the dynamic range of its output,  $V_{AFE}$ . The comparator,  $A_2$ , detects the level crossings and sends a signal ( $V_{COMP}$ ) to the switch control unit (SCU). The SCU in turn sends four non-overlapping signals ( $\phi_1-\phi_4$ ) to drive the switched capacitor,  $C_{SW}$ . This action injects a fixed amount of charge into the summing node of the integrator,  $\Sigma$ , as seen in Fig. 3. The charge injection causes a fixed voltage subtraction,  $\Delta V$ , at  $V_{AFE}$ , allowing  $A_1$  to continue integrating the photocurrent, as illustrated in Fig. 2. The circuit details of  $A_1$ ,  $A_2$ , and SCU are given in Fig. 4.

The digital logic was implemented on a Xilinx XC7A35T

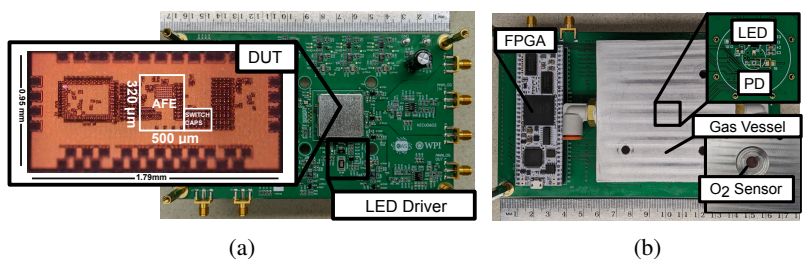


Fig. 5: (a) Micrograph and top side of eval board. (b) Bottom side of eval Fig. 6: a) Gas experiment physical testbench and board with FPGA and gas test vessel.

Mass Flow Controllers (b) Power Supply MFC/PC **Evaluation Board** Interface

(b) diagram.

FPGA, which controls power-up sequence, excitation and readout phase timing, front-end bias, and LED driver power. A significant role of the FPGA was the automatic "gain control" for the LED driver. The FPGA counts the number of comparator  $(A_2)$  pulses and adjusts the LED drive to ensure the number of pulses is the same for each measurement. For low PO<sub>2</sub>, the luminescent sensor emits many red photons for a given amount of exciting blue photons, so the LED drive current is set weaker. Conversely, the LED drive increases to excite more luminophores for high PO2. If the number of pulses from the AFE is less than a set threshold, the LED bias increases by one bit or vice versa. If the pulses match the threshold, there is no change. The automatic LED drive tuning expands the O<sub>2</sub> measurement dynamic range.

Fig. 4 contains simplified schematics of the AFE sub-blocks. The front-end amplifier,  $A_1$ , is a telescopic cascode with PMOS inputs with a common source output stage [11]. The time constant of the front end should be at least one order of magnitude less than the luminescent decay time to reduce the error induced from the front end to less than 1% [12]. The comparator, A<sub>2</sub>, performs the level crossing detection function of the sampler. The circuit detects when the output of the integrator reaches the threshold and triggers the switchedcapacitor circuit to inject a fixed amount of charge into the summing node of the op-amp and generate the voltage step  $(\Delta V)$ , depicted in Fig. 2.

To achieve narrow LED pulses, we employed a current steering technique inspired by emitter-coupled logic [13]. A regulated current source controls the tail current that sets the LED drive based on a bias voltage provided by the controller. The controller turns on the replica current path when the main control loop sends the command to excite the O<sub>2</sub> sensing film. This action wakes up the tail current source and establishes the LED drive current. Once the replica path establishes the LED driver current, the controller quickly switches to the active channel to excite the luminophores. The driver can set an LED pulse intensity up to 1 A with 10-bit resolution and pulse width as narrow as a few hundred nanoseconds.

#### IV. MEASUREMENT RESULTS

We implemented the AFE in TSMC's 180 nm 1P6M CMOS process. The inset in Fig. 5a is the die micrograph. The AFE active area is 0.16 mm<sup>2</sup>. Fig. 5 displays the evaluation board with the FPGA daughter card installed. We have conducted four majors tests with the prototype: 1-2) the bandwidth and input-referred noise to evaluate key front end performance; 3) a transient test to assess the hardware implementation of the  $\tau$ -estimation algorithm; and 4) a gas test to demonstrate the system's O<sub>2</sub> measurement performance.

During a 40  $\mu s$  excitation phase (30  $\mu s$  replica, 10  $\mu s$ active), the auxiliary LED driver uses a maximum of 15  $\mu J$ to excite the sensor at high PO2. During the excitation and readout phase (100  $\mu s$ ), the AFE uses 130 nJ to collect three samples for a  $\tau$  calculation. The input-referred noise and the bandwidth of  $A_1$  are given in Figs. 7a and 7b. The integrated noise is 124  $uV_{rms}$ , measured over a bandwidth from 200 Hz to 100 kHz, and the 1/f corner is  $\sim$  10 kHz. The measured gain-bandwidth product of the front-end amplifier is 10 MHz.

We calculated the  $\tau$  employing the proposed lifetime estimation algorithm using the time differences between comparator pulses,  $V_{COMP}$ . To assess the accuracy and precision of the technique, we fed the AFE with an exponentially decaying current with a controlled time constant,  $i_{test}$  in Fig. 7c. We measured each time constant ten times. We also calculated the lifetime by fitting an exponential model to the same stimulus current waveform for comparison. Fig. 8 shows the error between the proposed algorithm and the exponential model. For time constants ranging from 1 to 20  $\mu s$ , the relevant range for human transcutaneous  $O_2$  estimation, the mean error is  $\sim$ -1.9%, with the error bounds +1%/-4%. Increased error for  $t < 1\mu s$  is due to the comparator response delay. With a  $\Delta V$ of 0.7 V and a C<sub>F</sub> of 2 pF, the sampler requires a minimum of 3 pC to perform a calculation.

The in vitro gas test is a ratiometric mass flow rate experiment, explained in detail in [7]. We used the testbench, shown in Fig. 6, to test the O2 sensor over a range of PO2. To control the  $PO_2$ , we mixed  $O_2$  and nitrogen  $(N_2)$  in controlled ratios at 760 mmHg (1 atm). MKS 1179A mass flow controllers (MFC) set the gas mixture ratios. For fixed volume, temperature, and pressure, the partial pressure of a gas is directly related to the mass of the gas in the mixture. The PO2 was swept from 0 to 228 mmHg in 14.25 mmHg steps. A PC software controls the mass flow set points and the data readout.

The calculated time constants are plotted against PO<sub>2</sub> in Fig. 9a, and Fig. 9b is the Stern-Volmer plot of the same data. The deviation from the linear relationship at relatively high

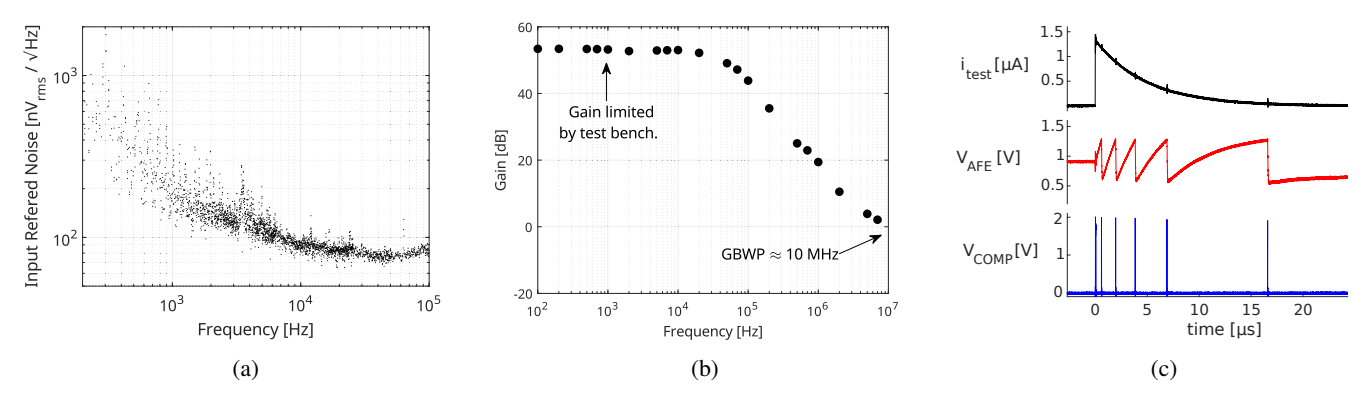


Fig. 7: Measured (a) input refered noise, (b) AC response, and (c) transient response.

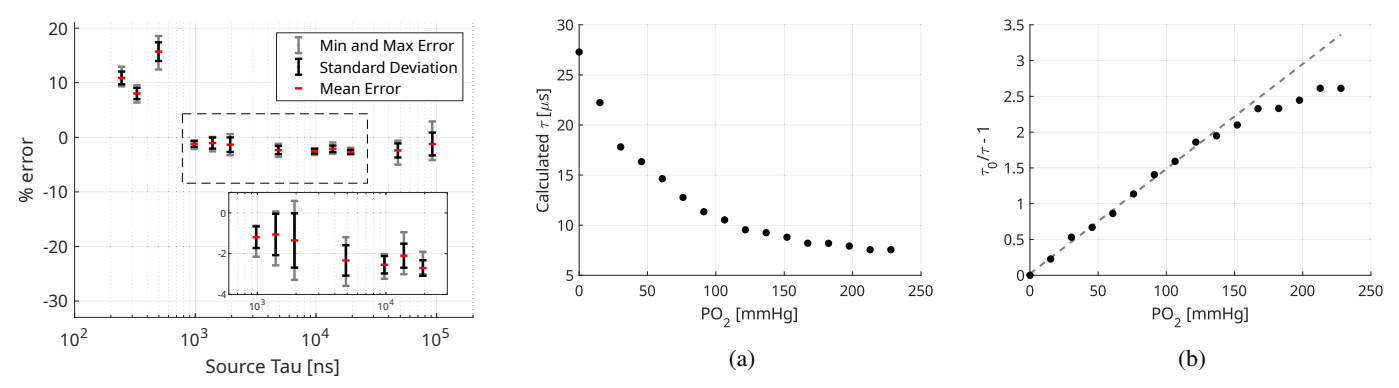


Fig. 8: Lifetime measurement error.

Fig. 9: (a) Calculated  $\tau$  from gas test. (b) Stern-Volmer plot.

 $PO_2$  is due to some luminophores being inaccessible to be quenched by  $O_2$  [14]. The nonuniform sampler can measure  $PO_2$  from 0 to 150 mmHg, covering the human-relevant range, with a 2.2 mmHg mean error, lower than the FDA standard of 5 mmHg [15]. Table I compares this work to prior art. A device for invasive deep tissue oxygenation measurement is presented in [16], with a slower sampling rate and smaller technology node, leading to lower power consumption.

# V. CONCLUSION

This work demonstrates for the first time, a hardware implementation of a nonuniform sampling technique and algorithm to extract the  $\tau$  of luminescent events, for the emerging application of noninvasive transcutaneous  $O_2$  measurements.

#### ACKNOWLEDGEMENTS

This work was supported in part by NSF ECCS-2143898.

TABLE I: Comparison of luminescent oxygen sensors.

	[4]	[2]	[16]	This work
	CICC '20	ACS '18	ISSCC '20	ESSCIRC '22
Tech (nm)	180	PCB	65	180
Area (mm <sup>2</sup> )	1.04	-	3.842	0.16 (AFE)
Power $(\mu W)$	632	-	140	835
$V_{DD}/V_{LED}$ (V)	1.8/5	-/-	1.2/-	1.8/5
Technique	Time	Intensity	Phase	Time
TransZ Gain	59 - 943 k $\Omega$	-	-	2 pF
Bandwidth	80 kHz	-	-	10 MHz*
Sample Rate	-	-	360 SPS	5 MSPS†
O <sub>2</sub> Error (mmHg)	-	-	-	2.2
Noise $(\mu V)$ ‡	-	-	-	124

<sup>\*</sup> Gain bandwidth product, † Maximum, ‡ Input referred

# REFERENCES

- [1] I. Costanzo *et al.*, "Respiratory monitoring: Current state of the art and future roads," *IEEE Rev. Biomed. Eng.*, vol. 15, pp. 103–121, 2022.
- [2] C. J. Lim et al., "Wearable, luminescent oxygen sensor for transcutaneous oxygen monitoring," ACS Applied Materials & Interfaces, vol. 10, no. 48, pp. 41 026–41 034, Jul 2018.
- [3] W. Weteringen et al., "Novel transcutaneous sensor combining optical tcPO2 and electrochemical tcPCO2 monitoring with reflectance pulse oximetry," Med. Biol. Eng. Comput., vol. 58, no. 2, pp. 239–247, 2020.
- [4] I. Costanzo *et al.*, "An integrated readout circuit for a transcutaneous oxygen sensing wearable device," in *CICC*, 2020, pp. 1–4.
- [5] T. B. Tufan et al., "A fluorescent thin film-based miniaturized transcutaneous carbon dioxide monitor." in BioCAS, 2021, pp. 1–5.
- [6] U. Guler et al., "Emerging blood gas monitors: How they can help with COVID-19," IEEE Solid-State Circuits Mag., vol. 12, pp. 33–47, 2020.
- [7] I. Costanzo et al., "A noninvasive miniaturized transcutaneous oxygen monitor," IEEE TBioCAS, vol. 15, no. 3, pp. 474–485, 2021.
- [8] M. Y. Berezin et al., "Fluorescence Lifetime Measurements and Biological Imaging," Chem. Rev., vol. 110, no. 5, pp. 2641–2684, May 2010.
- [9] M. Quaranta et al., "Indicators for optical oxygen sensors," Bioanalytical Reviews, vol. 4, no. 2, pp. 115–157, 2012.
- [10] R. J. Woods et al., "Transient digitizer for the determination of microsecond luminescence lifetimes," Anal. Chem., vol. 56, no. 8, pp. 1395–1400, 1984, pMID: 6465515.
- [11] J. R. Baker, CMOS Circuit Design, Layout, and Simulation, 3rd ed. Piscataway, NJ: IEEE Press, 2010.
- [12] H. Johnson et al., Calculation of Rise Time. Prentice-Hall, Inc., 1993, pp. 399–407.
- [13] M. Thompson et al., "High power laser diode driver based on power converter technology," *IEEE Trans. Pow. Elec.*, vol. 12, pp. 46–52, 1997.
- [14] J. R. Lakowicz, Principles of fluorescence spectroscopy, 3rd ed. New York: Springer, 2006.
- [15] "Cutaneous Carbon Dioxide (PcCO2) and Oxygen (PcO2) Monitors -Guidance," U.S. Food and Drug Administration, Dec 2018.
- [16] S. Sonmezoglu *et al.*, "34.4 a 4.5mm3 deep-tissue ultrasonic implantable luminescence oxygen sensor," in *ISSCC*, 2020, pp. 454–456.